International Journal of Machine Tools and Manufacture, 163, 103702, Apr 2021,
DOI https://doi.org/10.1016/j.ijmachtools.2021.103702

A machining test to evaluate thermal influence on the kinematics of a five-axis machine tool

Soichi Ibaraki *, Rin Okumura
Graduate School of Advanced Science and Engineering, Hiroshima University, Kagamiyama 1-4-1, Higashi-Hiroshima, 739-8527, Japan

A B S T R A C T

The thermal deformation of a machine tool, typically caused by environmental temperature variations or the heat generated by a rotating spindle, often changes the position and orientation errors of the rotary axis average lines. By applying kinematic modeling of a five-axis machine tool, this paper shows that they can be estimated from the finished geometry of any test piece, provided that the test piece contains the features that are sufficiently sensitive to them. Based on the kinematic analysis of their influence, a new machining test is proposed to evaluate the thermal influence on the position and orientation errors of the rotary axis average lines. By inversely solving the five-axis kinematic model, this paper shows that the position and orientation errors of the rotary axis average lines can be analytically identified by the finished test piece geometry. An experimental case study demonstrates that the position and orientation errors of the rotary axis average lines, which change due to the thermal influence, can be observed from the finished test piece geometry.

Keywords: Machine tool Thermal error Machining test Five-axis Kinematics

1. Introduction

The thermal deformation of machine tools, which is typically caused by a variation in the environmental temperature, the heat generated by a rotating spindle, or moving the linear or rotary axes, is often one of the critical machining error contributors. As described in [1]-[4], numerous efforts have been focused on reporting the measurement, modeling, and compensation of thermal errors. For machine tool builders or users that evaluate the thermal influence on a machine's positioning accuracy for a variety of thermal conditions, ISO 230-3 [5] and its machine-specific counterparts, such as ISO 10791-10 [6] for machining centers, describe the standardized thermal tests. They describe several tests to evaluate the thermal influence on the 3D position and orientation of a tool that is positioned at a single point (or at most, three points) in the workspace.

Although a non-cutting geometric test is indispensable, many machine tool users wish to evaluate a machine's performance with a machining test. ISO 10791-7 [7] describes the machining tests for machining centers. The influence of the machine geometric errors on the cone frustum test piece [8][9] and the S-curve test piece [10][11], which are included in ISO 10791-7 [7], have been studied by many researchers. Recent studies have proposed machining tests that enable a user to numerically identify all the position and orientation errors of the rotary axis average lines, which are typical error sources with five-axis kinematics. Ibaraki et al. [12][13] presented a pyramid-shaped machining test, and the test proposed by Velenosi et al. [14] was analogous. Ibaraki et al. [15] and Jiang et al. [16] presented a simpler set of machining tests based on the same principle. Morimoto et al. [17] presented a machining test based on a non-rotating tool. Ibaraki et al. [18] presented a machining test for turning operations with the angular indexing of a test piece. Arizmendi et al. [19] analyzed the influence of the machine's geometric errors on five-axis machined elliptical dimples.

All of the machining tests reviewed above evaluate the geometric accuracy of a single finished test piece, assuming

that a machine is in a thermally stable condition after sufficient warm-up. The evaluation of thermal influence on the machine's accuracy is beyond their scope. When a machine is in the initial thermal state, by repeatedly performing the same machining operation, one may observe a change in the geometric accuracy of the finished test pieces, which is typically caused by the thermal influence. This machining test is sometimes performed by a machine tool builder for machine performance inspection. However, no ISO standard describes such a machining test. In the literature, a few proposals can be found; Wiessner et al. [20] proposed a five-axis machining test, which, unlike the test presented in this study, targets a single rotary axis, e.g., a rotary table, and cannot be applied to two rotary axes on a single test piece. It can include a turning operation, where the rotary axis becomes a heat source. Ibaraki et al. [12] applied a pyramid-shaped machining test to evaluate the thermal error. The test presented in this investigation builds upon it so it has better applicability to thermal tests. The test in [12] requires a cubic test piece. To apply it to the thermal test, when one test piece is finished, it should be replaced with a new unmachined one for the next round. The test presented in this study consists of three steps for each round, and one test piece can have four sets. Höfer et al. [21] and Ibaraki et al. [22] presented a thermal machining test for the positioning of a linear axis. Thermal influence on linear axis geometric errors can be observed by a simpler machining test. ISO 26303 [23] describes a short-term capability test for machine tools in which a sample batch of test pieces is repeatedly machined. Its objective is to conduct a statistical process control analysis for a large batch production; the evaluation of the thermal distortion is beyond its scope.

The kinematic modeling theory, which is well-developed for the error compensation or the indirect error identification for five-axis machine tools [24], can analytically formulate the relationship between the finished geometry of any test piece and the position and orientation errors of the rotary axis average lines. Therefore, any test piece can be used to estimate the position and orientation errors of the rotary axis average lines, provided that the test piece contains the features that are machined at different angular positions of the rotary axes and are sufficiently sensitive to the position and orientation errors of the rotary axis average lines. Although many researchers have proposed different machining tests, this viewpoint is missing in many studies. Numerous studies, e.g., [14][16][17][20], have analytically formulated the geometric errors of their test pieces, and all can be derived from the machine's kinematic model presented in this paper.

Herein, this paper presents a machining test to evaluate the thermal influence on the position and orientation errors of the rotary axis average lines. Heat is generated mainly by a spindle rotation and the environmental thermal change. The original contributions of this investigation are as follows: 1) The application of the machine kinematic modelling to the analytical formulation of the workpiece geometric errors under the position and orientation errors of the rotary axis average lines is presented. It can be applied to any five-axis machined workpieces. This paper proposes a thermal five-axis machining test. By applying the machine kinematic model, an algorithm is presented to identify position and orientation errors of rotary axis average lines from the measured geometry of the finished test piece. 2) Similar to many other indirect calibration schemes, e.g., the R-test, the linear axis error motions can significantly influence the uncertainty in the estimated rotary axis geometric errors. The uncertainty analysis is presented to study their influence.

This study clarifies that the geometric errors of the finished test pieces can be analytically formulated as a function of the rotary axis location errors by applying the five-axis kinematic model, which provides an algorithm to identify the rotary axis location errors from the finished test piece geometry. The present machining test is designed such that

each face is machined at every combination of B'=-90°, 0°, and +90° and C'= 0°, 90°, 180°, and 270°. Thus, the sensitivity of the finished test piece's geometry to the rotary axis location errors can be maximized within these angular ranges.

2. Formulation of workpiece geometric errors under rotary axis geometric errors

This study considers a five-axis machine configuration with a rotary table C'-axis mounted on a swivel B'-axis (see Fig. 3); however, an analogous formulation applies to all the five-axis machine configurations.

A local coordinate system (CS) rotates with the B'- and C'-axes, and its Z-axis is aligned with the actual C'-axis of rotation; this is referred to as the workpiece CS (WCS). Since the test piece is fixed on the WCS, its geometry is determined via the tool center point (TCP) trajectory in the WCS. Negligibly small error motions of the linear axes are assumed in this study (Section 6 will discuss the contribution of the linear axis error motions to the uncertainty), which means that the TCP trajectory is given and there is no error in the machine coordinate system (MCS). In this paper, the MCS is the fixed coordinate system with its origin at the nominal intersection of the B'- and C'-axes. Therefore, the geometry of the finished test piece can be formulated by converting the TCP trajectory from the MCS to the WCS. In other words, the finished test piece geometry shows the position and orientation of the WCS, which are equivalent to the position and orientation of the B'- and C'-axis average lines.

Based on this principle, any test piece geometry enables a user to identify the position/orientation of the B'- and C'-axis average lines, provided that it contains the features that are machined at the B'- and C'-axis angular positions in which the position/orientation of the B'- and C'-axis average lines are observable.

This paper considers the position and orientation errors of the rotary axis average lines, shown in Table 1 ("error sources"), as sources for the geometric errors of the finished test piece. See ISO 230-1 [25] for the definition of the position and orientation errors of the rotary axis average lines. The axis average line of a rotary axis represents the "mean" position and orientation of the axis of rotation over its the full rotation. The variation in the position and orientation of the axis of rotation from the axis average line is called *error motions* of a rotary axis in ISO 230-1 [25]. The formulation presented in this section can be extended to error motions in a straightforward manner.

The relationship of the position and orientation errors of the rotary axis average lines to the geometric errors of the finished workpiece can be formulated using the five-axis kinematic model. It is a well-developed theory and is adopted in many previous works (a review can be found in [24]), and its detailed derivation is not presented in this paper. This study shows that the position/orientation of the machined feature can be analytically formulated by applying the following simplified representation that was presented by Ibaraki et al. [26] in a straightforward manner. This is a major contribution of this study.

When the nominal TCP position is given by ${}^{w}p^{*}\in\Re^3$ in the WCS, its actual position in the WCS, ${}^{w}p\in\Re^3$, under the error sources in Table 1, is formulated as follows.

$$\begin{bmatrix} {}^{w}\boldsymbol{p} \\ \mathbf{1} \end{bmatrix} \approx \boldsymbol{D_x}(\Delta\boldsymbol{x})\boldsymbol{D_y}(\Delta\boldsymbol{y})\boldsymbol{D_z}(\Delta\boldsymbol{z})\boldsymbol{D_a}(\Delta\boldsymbol{a})\boldsymbol{D_b}(\Delta\boldsymbol{b})\boldsymbol{D_c}(\Delta\boldsymbol{c}) \begin{bmatrix} {}^{w}\boldsymbol{p}^{*} \\ \mathbf{1} \end{bmatrix} \tag{1}$$

where

$$\Delta x = -(\delta x_{BR}^{0}\cos b + \delta z_{BR}^{0}\sin b + \delta x_{CB}^{0})\cos c + \delta y_{BR}^{0}\sin c \tag{2}$$

$$\Delta y = -(\delta x_{BR}^{0}\cos b + \delta z_{BR}^{0}\sin b + \delta x_{CB}^{0})\sin c - \delta y_{BR}^{0}\cos c \tag{3}$$

$$\Delta z = \delta x_{BR}^{0} \sin b - \delta z_{BR}^{0} \cos b \tag{4}$$

$$\Delta a = -(\alpha_{BR}^{0} \cos b + \gamma_{BR}^{0} \sin b + \alpha_{CB}^{0}) \cos c + \beta_{BR}^{0} \sin c \tag{5}$$

$$\Delta b = -(\alpha_{BR}^{0} \cos b + \gamma_{BR}^{0} \sin b + \alpha_{CB}^{0}) \sin c - \beta_{BR}^{0} \cos c \tag{6}$$

$$\Delta c = \alpha_{BR}^{0} \sin b - \gamma_{BR}^{0} \cos b \tag{7}$$

In Eq. (1), $D_*(\dagger) \in \Re^{4\times4}$ represents the homogeneous transformation matrix, which represents the translation in the X, Y, or Z directions (*=x, y, z) or the rotation around the X-, Y-, or Z-axis (*=a,b,c), and it is described in [26].

$$\mathrm{D_x(x)} = \begin{bmatrix} 1 & 0 & 0 & x \\ 0 & 1 & 0 & 0 \\ 0 & 0 & 1 & 0 \\ 0 & 0 & 0 & 1 \end{bmatrix},\ \mathrm{D_y(x)} = \begin{bmatrix} 1 & 0 & 0 & 0 \\ 0 & 1 & 0 & y \\ 0 & 0 & 1 & 0 \\ 0 & 0 & 0 & 1 \end{bmatrix},\ \mathrm{D_z(z)} = \begin{bmatrix} 1 & 0 & 0 & 0 \\ 0 & 1 & 0 & 0 \\ 0 & 0 & 1 & z \\ 0 & 0 & 0 & 1 \end{bmatrix} \tag{8}$$

$$\mathrm{D_a(a)} = \begin{bmatrix} 1 & 0 & 0 & 0 \\ 0 & \cos a & -\sin a & 0 \\ 0 & \sin a & \cos a & 0 \\ 0 & 0 & 0 & 1 \end{bmatrix},\ \mathrm{D_b(b)} = \begin{bmatrix} \cos b & 0 & \sin b & 0 \\ 0 & 1 & 0 & 0 \\ -\sin b & 0 & \cos a & 0 \\ 0 & 0 & 0 & 1 \end{bmatrix},\ \mathrm{D_c(c)} = \begin{bmatrix} \cos c & -\sin c & 0 & 0 \\ \sin c & \cos c & 0 & 0 \\ 0 & 0 & 1 & 0 \\ 0 & 0 & 0 & 1 \end{bmatrix}$$

The left-hand-side superscript, w, in ${}^{w}p$, indicates that the vector is in the WCS. In addition, b and c denote the angular positions of the B' and C' axes, respectively.

This formulation is particularly useful for formulating the test piece's geometric errors. Equation (1) shows that the actual TCP position in the WCS, ${}^{w}p$, is given by rotating its nominal position, ${}^{w}p^{*}$, around Z, Y, and X-axis of the WCS, respectively by Δc, Δb, and Δa, and then by linearly moving it to Z, Y, and X directions by Δz, Δy, and Δx. When a feature (e.g. a face) on the finished test piece is machined at the angular position of B'- and C'-axes, b and c, its position and orientation errors is given by (Δx, Δy, Δz, Δa, Δb, Δc).

The application of this formulation to the machining test proposed in this paper will be presented in Section 3.3. It will illustrate the usefulness of Eq. (1) for the error source diagnosis from the workpiece geometric errors.

Table 1. Position and orientation errors of the rotary axis average lines and the assessed uncertainties under the uncertain contributors in Table 7.

Error sources	Symbol		Uncertainty (k=2)
	[24]	[25]	
Position error in X of B-axis [μm]	$\delta x_{BR}{}^{0}$	E_{X0B}	6.0
Position error in Y of C-axis [μm]	$\delta y_{BR}{}^{0}$	E_{Y0C}	8.4
Position error in Z of B-axis [μm]	$\delta z_{BR}{}^{0}$	E_{Z0B}	2.6
Intersection error of C- to B-axis [μm]	$\delta x_{CB}{}^{0}$	$E_{X(0B)C}$	29.4
Parallelism error around X of B- to Y-axis [μm/m]	$\alpha_{BR}{}^{0}$	E_{A0B}	6
Squareness error of C- to X-axis at B0 [μm/m]	$\beta_{BR}{}^{0}$	E_{B0C}	124
Parallelism error around Z of B- to Y-axis [μm/m]	$\gamma_{BR}{}^{0}$	E_{C0B}	168
Squareness error of C- to B-axis [μm/m]	$\alpha_{CB}{}^{0}$	$E_{A(0B)C}$	36

3. Proposed test procedure and error source identification

3.1. Proposed test procedure

Figure 1 shows the nominal geometry of the finished test piece, where the finished faces are represented by the symbol $S_{n,m,*}$. The faces are named by the following three parameters:

1) step number, *n*=1, … , 12 (top-most: 1);

2) its location; *m*=1, … , 4 is 1 for the –Y side face, 2 is for the +X side face, 3 is for the +Y side face, and 4 is for the –X side face;

3) side or bottom face where * is “s” for the side face and “b” is for the bottom face.

To cover the entire rotation stroke of B’ and C’ axes, and to easily measure the finished test piece, the faces in the proposed test piece are machined by every combination of C’=0°, 90°, 180°, and 270° and B’ = -90°, 0°, and 90°. Figure 2 shows a set of three steps, each of which is finished by the B’- and C’-axis angular positions that are presented in Table 2. The test design principle can be summarized as follows:

- The first square, whose faces are all machined at B’=C’=0°, is the reference for the measurement (see Fig. 3 a).
- In the second square, two of its faces are machined at B’=0° and C’=0°, and the other two are machined at B’=0° and C’=180° (see Fig. 3 b), to identify the position and orientation errors of the C’-axis average line.
- On the third square, each face is machined at either B’=-90° or 90° (see Fig. 3 c) to identify the position and orientation errors of the B’-axis average line.

This set of three steps is called the first set. When the first set is finished, at the retracted Z position, the spindle is rotated at a constant speed or a variable speed spectrum for 15 min to warm up the machine. This is repeated until a total of four sets (12 steps) are machined.

The detailed test procedure is shown in the flow chart in Fig. 4.

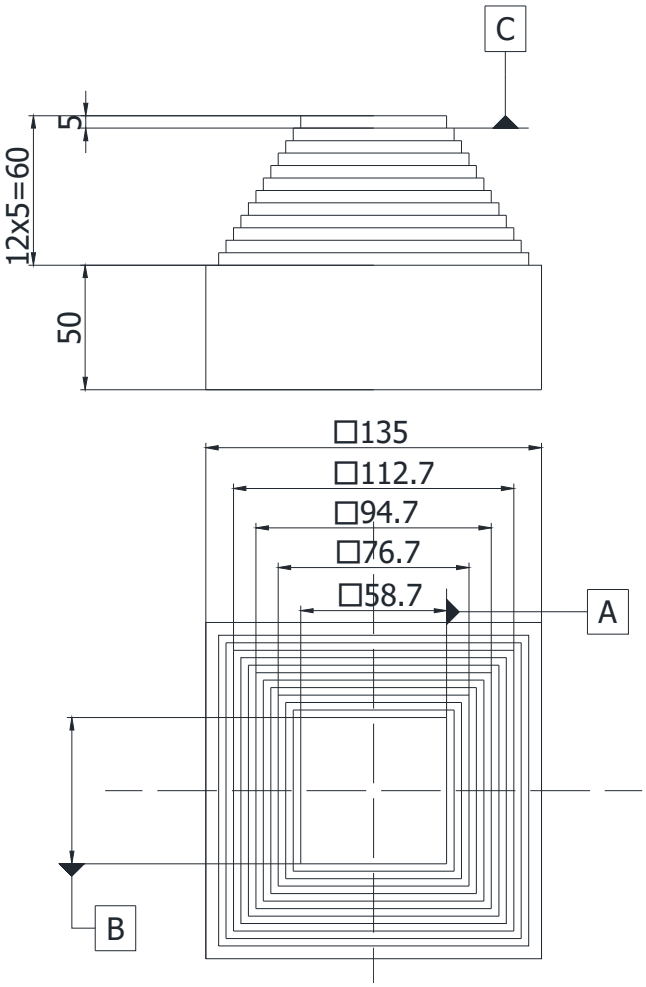

Figure 1. Finished test piece geometry. A, B, and C represent the datum planes (see Section 3.2).

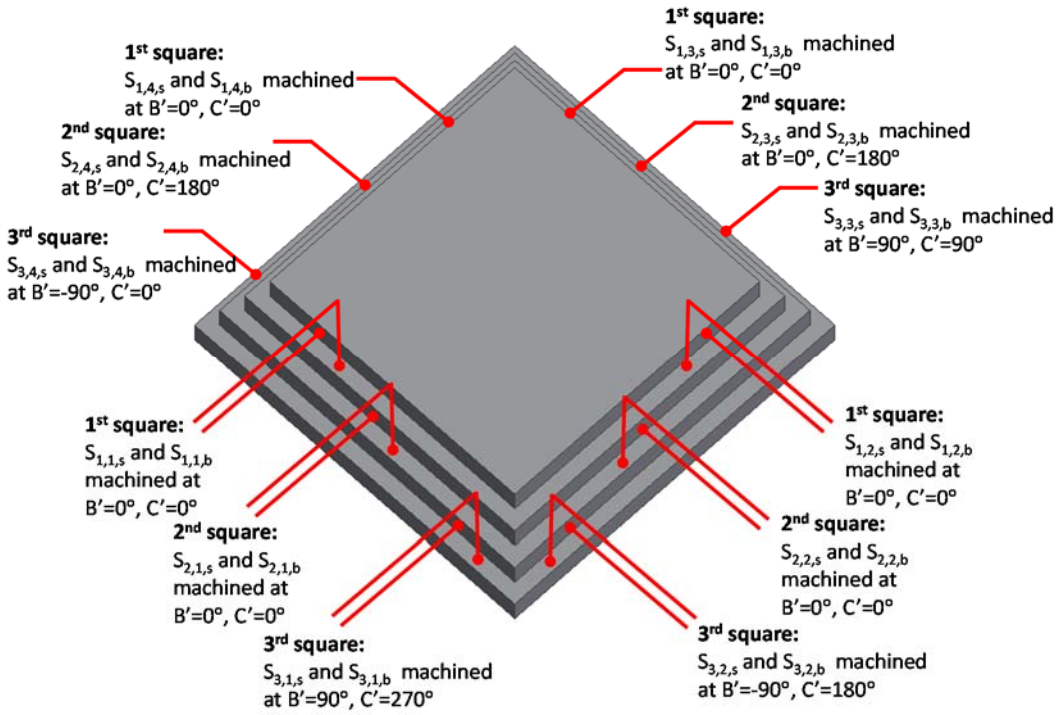

Figure 2. Finished test piece geometry of one set, which consists of three-square steps. Each face is machined at B'- and C'-axis angular positions. $S_{n,m,*}$ represents the finished face, where *n* is the step number, *m* represents its location, and * is the side or bottom face (s or b) (see Section 3.1).

Table 2. Correspondence of the faces of the finished test piece to the B'- and C'-axis angular positions (see Figure 2).

Step	Faces	B'- and C'-angles
1st	$S_{1,1,s/b}$, $S_{1,2,s/b}$, $S_{1,1,s/b}$, $S_{1,1,s/b}$	B'=0°, C'=0°
2nd	$S_{2,1,s/b}$, $S_{2,2,s/b}$	B'=0°, C'=0°
	$S_{2,1,s/b}$, $S_{2,2,s/b}$	B'=0°, C'=180°
3rd	$S_{3,4,s/b}$	B'=-90°, C'=0°
	$S_{3,2,s/b}$	B'=-90°, C'=180°
	$S_{3,1,s/b}$	B'=+90°, C'=270°
	$S_{3,3,s/b}$	B'=+90°, C'=90°

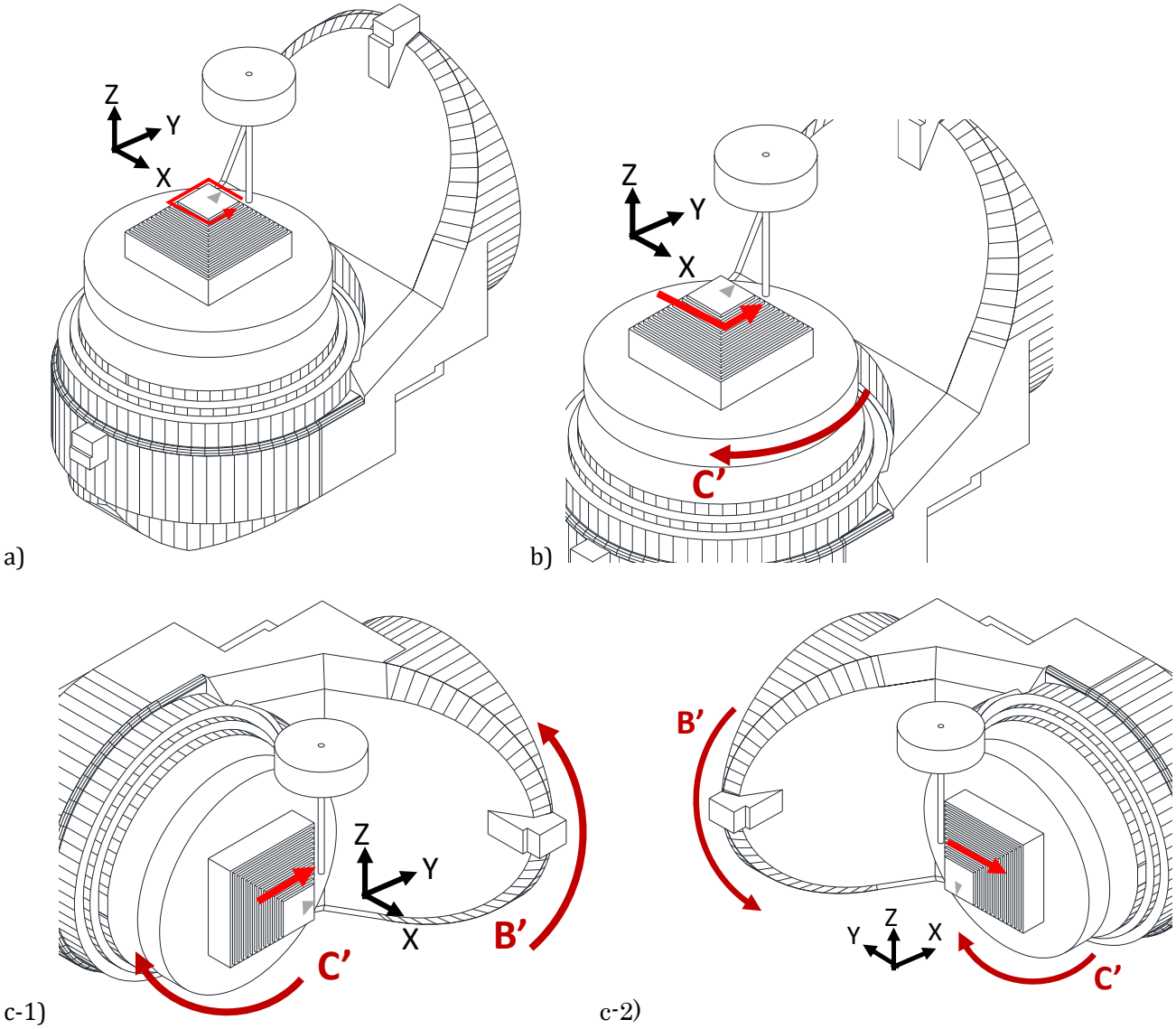

Figure 3. Machining procedure [27]. a) First step: four faces, $S_{1,1,s/b}$ to $S_{1,4,s/b}$, are machined at B'=C'=0°. a) Second step: two faces, $S_{2,1,s/b}$ and $S_{2,2,s/b}$, are machined at B'=C'=0°, and then the opposite faces, $S_{2,3,s/b}$ and $S_{2,4,s/b}$, are machined at C'=180°. c-1) Third step: one face, $S_{3,4,s/b}$, is machined at B'=-90° and C'=0°, and then the opposite face, $S_{3,2,s/b}$, is machined at B'=-90° and C'=180°. c-2) Third step: at B'=+90° and C'=270°, $S_{3,1,s/b}$ is machined, and then the opposite face, $S_{3,3,s/b}$, is machined at B'=+90° and C'=90°.

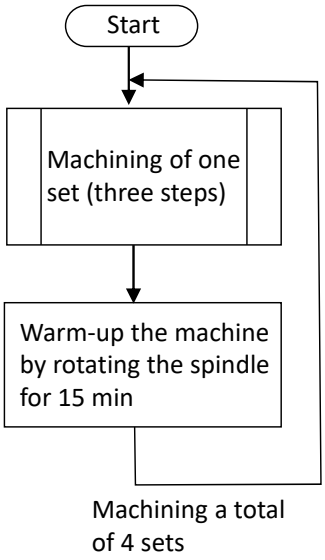

< Machining of one set (three steps) >

1st square step

Four faces, $S_{1,m,*}$ (m=1, …, 4 and *=s/b), are machined at B'=C'=0° by feeding an end mill to either the X- and Y-direction (see Fig. 3 a).

2nd square step

At B'=C'=0°, two faces, $S_{2,1,s/b}$ and $S_{2,2,s/b}$, are finished by feeding toward the X- then the Y-directions (see Fig. 3 b).

Rotate C'-axis by 180°. Then two faces, $S_{2,3,s/b}$ and $S_{2,4,s/b}$, are finished similarly by feeding toward the X- and then the Y-direction.

3rd square step

The faces, $S_{3,4,s/b}$, are finished at B'=-90° and C'=0° by feeding toward the Y-direction (see Fig. 3 c-1).

The faces, $S_{3,2,s/b}$, are finished at B'=-90° and C'=180°.

The faces, $S_{3,1,s/b}$, are finished at B'=+90° and C'=270° (see Fig. 3 c-2).

The faces, $S_{3,3,s/b}$, are finished at B'=+90° and C'=90°.

Return

Figure 4. Machining test procedure.

3.2. Measurement

The finished test piece geometric errors that are shown in Table 3 are measured. The error symbols in Table 3 represent the following. When considering $\delta y(S_{n,1,s}, S_{1,1,s})$, δy represents the error direction, which is the position error in the X-, Y-, or Z-direction (δx, δy, δz) or the orientation error around the X, Y, or Z-axis (α, β, γ). The first symbol in the parenthesis, $S_{n,1,s}$, represents the surface of the error, and the second symbol, $S_{1,1,s}$, represents the reference surface.

This section describes the measurement procedure. The measurement is performed using either a coordinate measuring machine (CMM) or an on-machine measurement that uses a touch-trigger probe. When the finished test piece is unclamped for the CMM measurement, one should be careful with unclamping's influence on the deformation of the test piece [14]. For the on-machine measurement, the finished test piece should not be unclamped, and all the points should be measured at B'=C'=0°.

First, the measurement CS is defined as follows:

- Define the datum plane C in Fig. 1 by probing multiple points on it, and take the best-fit plane.
- Probe multiple points on the machined surfaces $S_{1,2,s}$ and $S_{1,4,s}$ in their longitudinal direction to calculate their projected lines on the datum plane C. Define the datum plane B in Fig. 1 such that it contains their symmetry line and is perpendicular to the datum surface C. Define the X-axis to measure the CS by the intersection of the datum planes B and C.
- Y-axis of the measurement CS is on the datum plane C, and it is perpendicular to the X-axis.

Subsequently, all the machined faces are probed. Figure 5 shows examples of the probed points. The pitch of the probed points, p, should be chosen to measure the position and orientation of each machined face while minimizing the influence of the surface roughness or waviness.

The geometric errors in Table 3 are defined in compliance with ISO 1101 [26]. Among them, the position error of one surface to the other surface is defined as follows. The position error for Y from $S_{n,3,s}$ to $S_{n,1,s}$ (n=2, 5, 8, 11), $\delta y(S_{n,3,s}, S_{n,1,s})$, is taken as an example (see Fig. 6 a):

- Calculate the line of best-fit for the probed points on $S_{n,3,s}$. Subsequently, calculate the intersection point of this line to the YZ-plane of the measurement CS.
- Similarly, calculate the intersection point of the line of best-fit to the probed points on $S_{n,1,s}$ and the YZ-plane.
- The position error in Y of $S_{n,3,s}$ to $S_{n,1,s}$, $\delta y(S_{n,3,s}, S_{n,1,s})$ is an error in the distance between these two points, which is projected onto the XY plane, from its nominal value.

Similarly, as an example of the angular errors, the parallelism error around Y of $S_{n,1,b}$ to $S_{1,1,b}$ (n=1, 4, 7, 10), $\beta(S_{n,1,b}, S_{1,1,b})$, is calculated as follows (see Fig. 6 b):

- Calculate the lines of best-fit for the probed points on $S_{n,1,b}$, and those on $S_{1,1,b}$.
- The angle between them, when projected onto the ZX plane, is $\beta(S_{n,1,b}, S_{1,1,b})$.

Remark: In Table 3, six geometric errors associated with the first step of each set are influenced by the linear axis error motions only. For example, the perpendicularity of $S_{n,4,s}$ to $S_{n,1,s}$, $\gamma(S_{n,4,s}, S_{n,1,s})$ is dominated by the squareness error of the Y- to X-axis. The perpendicularity of $S_{n,2,s}$ to $S_{n,1,s}$, $\gamma(S_{n,2,s}, S_{n,1,s})$, that of $S_{n,4,s}$ to $S_{n,3,s}$, $\gamma(S_{n,4,s}, S_{n,3,s})$, and that of $S_{n,2,s}$ to $S_{n,3,s}$, $\gamma(S_{n,2,s}, S_{n,3,s})$ are all caused by the squareness error of the Y- to X-axis. However, other error motions,

e.g., the angular error motions of the X- or Y-axis, may cause minor differences. Table 4 summarizes this geometric error, which has the same error sources, and it can be evaluated as an alternative.

Table 3. Geometric errors of the finished test piece. $S_{n,m,*}$ represents the finished face, where *n* is the step number, *m* represents its location, and * represents the side or bottom face (s or b) (see Section 3.1).

	Symbol	Description
First step of each set (*n*=1, 4, 7, 10)	$\delta y(S_{n,1,s}, S_{1,1,s})$	Position error in Y of $S_{n,1,s}$ to $S_{1,1,s}$
	$\delta x(S_{n,4,s}, S_{1,4,s})$	Position error in X of $S_{n,4,s}$ to $S_{1,4,s}$
	$\gamma(S_{n,4,s}, S_{n,1,s})$	Perpendicularity of $S_{n,4,s}$ to $S_{n,1,s}$
	$\delta z(S_{n,1,b}, S_{1,1,b})$	Position error in Z of $S_{n,1,b}$ to $S_{1,1,b}$
	$\beta(S_{n,1,b}, S_{1,1,b})$	Parallelism around Y of $S_{n,1,b}$ to $S_{1,1,b}$
	$\alpha(S_{n,2,b}, S_{1,2,b})$	Parallelism around X of $S_{n,2,b}$ to $S_{1,2,b}$
Second step of each set (*n*=2, 5, 8, 11)	$\delta y(S_{n,3,s}, S_{n,1,s})$	Position error in Y of $S_{n,3,s}$ to $S_{n,1,s}$
	$\delta x(S_{n,4,s}, S_{n,2,s})$	Position error in X of $S_{n,4,s}$ to $S_{n,2,s}$
	$\beta(S_{n,3,b}, S_{n,1,b})$	Parallelism around Y of $S_{n,3,b}$ to $S_{n,1,b}$
	$\alpha(S_{n,4,b}, S_{n,2,b})$	Parallelism around X of $S_{n,4,b}$ to $S_{n,2,b}$
Third step of each set (*n*=3, 6, 9, 12)	$\delta y(S_{n,3,s}, S_{n,1,s})$	Position error in Y of $S_{n,3,s}$ to $S_{n,1,s}$
	$\delta x(S_{n,4,s}, S_{n,2,s})$	Position error in X of $S_{n,4,s}$ to $S_{n,2,s}$
	$\gamma(S_{n,4,s}, S_{n,3,s})$	Perpendicularity of $S_{n,4,s}$ to $S_{n,3,s}$
	$\delta z(S_{n,4,b}, S_{n,1,b})$	Position error in Z of $S_{n,4,b}$ to $S_{n,1,b}$
	$\alpha(S_{n,4,b}, S_{n,2,b})$	Parallelism around X of $S_{n,4,b}$ to $S_{n,2,b}$

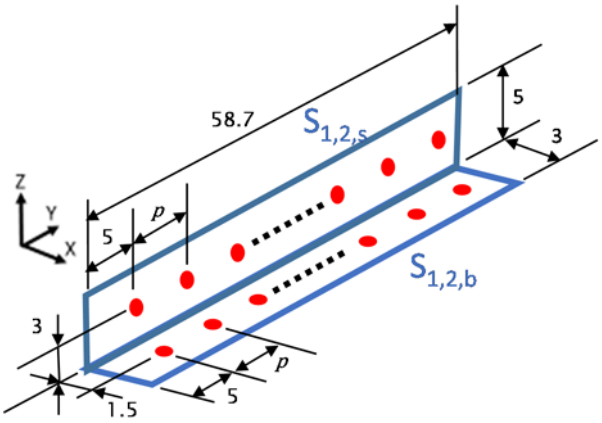

Figure 5. Example of the probed points (for the surfaces $S_{1,2,s}$ and $S_{1,2,b}$). *p* represents the pitch of the probed positions.

Table 4. Alternative geometric errors for the first step that have the same error sources; thus, it can be evaluated as an alternative.

	Errors in Table 3	Alternative errors that can be evaluated
First step of each set (n=1, 4, 7, 10)	$\delta y(S_{n,1,s}, S_{1,1,s})$	$\delta y(S_{n,3,s}, S_{1,3,s})$
	$\delta x(S_{n,4,s}, S_{1,4,s})$	$\delta x(S_{n,2,s}, S_{1,2,s})$
	$\gamma(S_{n,4,s}, S_{n,1,s})$	$\gamma(S_{n,2,s}, S_{n,1,s})$, $\gamma(S_{n,4,s}, S_{n,3,s})$, $\gamma(S_{n,2,s}, S_{n,3,s})$
	$\delta z(S_{n,1,b}, S_{1,1,b})$	$\delta z(S_{n,2,b}, S_{1,2,b})$, $\delta z(S_{n,3,b}, S_{1,3,b})$, $\delta z(S_{n,4,b}, S_{1,4,b})$
	$\beta(S_{n,1,b}, S_{1,1,b})$	$\beta(S_{n,3,b}, S_{1,3,b})$
	$\alpha(S_{n,2,b}, S_{1,2,b})$	$\alpha(S_{n,4,b}, S_{1,4,b})$

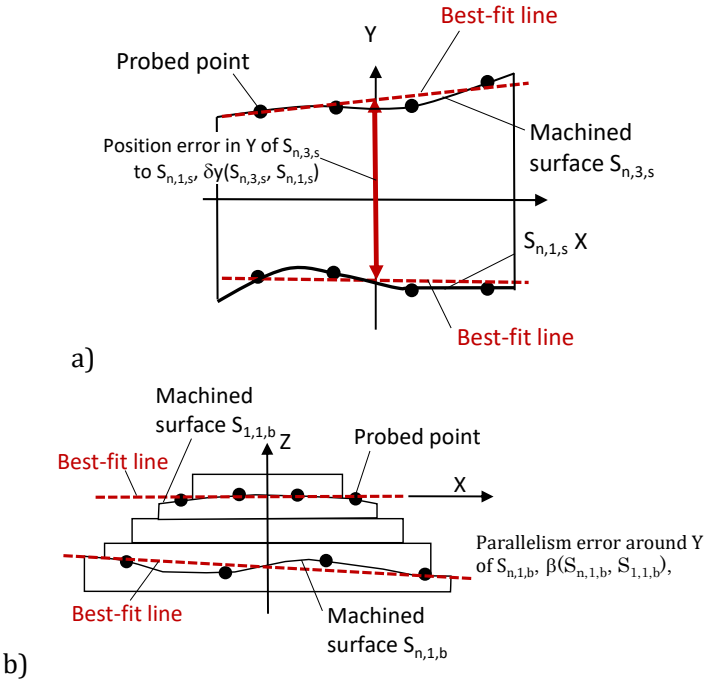

Figure 6. Definition of the examples for the geometric errors of the finished test piece. a) The position error in Y of $S_{n,3,s}$ to $S_{n,1,s}$, $\delta y(S_{n,3,s}, S_{n,1,s})$ is defined by the position of the line of best-fit to the probed points on the machined side faces, $S_{n,3,s}$ with respect to the line of best-fit to $S_{n,1,s}$. b) The parallelism error around Y of $S_{n,1,b}$ to $S_{1,1,b}$, $\beta(S_{n,1,b}, S_{1,1,b})$ is defined by the angle of the line of best-fit to the probed points on the machined bottom faces, $S_{n,1,b}$, to the line of best-fit to $S_{n,1,1}$

3.3. Identification of the position/orientation errors of the rotary axis average lines

The machine kinematic model, given in Eq. (1), can be applied to derive the kinematic relationship of the geometric errors of the finished test piece, shown in Table 3, and the rotary axis location errors in Table 1.

First, the formulation below assumes that there is no error motion other than the rotary axis location errors in Table 1. The influence of the linear axis error motions is analyzed in Section 6. This assumption is needed for any test scheme that measures the relative displacement of the TCP to the work table (see Remark 1 in Section 6). The angular positioning error motions of the B' and C' axes, E_{BB}, and E_{CC} can be identified for C'=0°, 90°, 180°, and 270° and B'=-90°, 0°, and 90° from the geometry of the finished test piece; however, they are not targeted in the scheme below. The radial, axial, and tilt error motions of the B' and C' axes, which represent the angle-dependent variation in the position and orientation of the axis of rotation from its axis average line [25], are also assumed to be sufficiently small.

Under these assumptions, the test piece's geometric errors, shown in Table 3, can be formulated by applying Eq. (1).

Example 1: $\beta(S_{n,3,b}, S_{n,1,b})$ (n=2, 4, 7, 10) in Table 3, the parallelism error around Y of $S_{n,3,b}$ to $S_{n,1,b}$, can be derived as follows. For the second step, the face, $S_{n,1,b}$, is machined at B'=C'=0°. Its orientation in the WCS around the Y-axis, which is denoted by $b_{n,1,b}$, is given by Δb in Eq. (6) with b=c=0°, i.e. $b_{n,1,b} = -\beta^0_{BR}$. By analogously formulating $b_{n,3,b}$ for the machining at C=180°, Eq. (12) can be derived.

Example 2: $\delta z(S_{n,4,b}, S_{n,1,b})$ (n=3, 6, 9, 12) in Table 3, the position error in Z of $S_{n,4,b}$ to $S_{n,1,b}$, can be derived as follows. For the third step, the bottom face, $S_{n,1,b}$, is machined at B'=+90° and C'=270°. Its mean Z position in the WCS, which is denoted by $z_{n,1,b}$, is described as follows.

$$z_{n,1,b} = \Delta z - \Delta b \cdot x_{n,1,b} + \Delta a \cdot y_{n,1,b} = \delta x^0_{BR} - \beta^0_{BR} \cdot y_{n,1,b} \quad (9)$$

where Δz, Δa, and Δb are given in Eqs. (4), (5), and (6) where b=90° and c=270°. $z_{n,m,*}$ ($x_{n,m,*}$, $y_{n,m,*}$) represents the nominal Z (X, Y) position of the surface $S_{n,m,*}$. Note that the mean X position of the face $S_{n,1,b}$ is zero, i.e., $x_{n,1,b}$=0. By analogously formulating $z_{n,4,b}$, the mean Z position of the face $S_{n,4,b}$, which is machined at b=-90° and c=0°, results in Eq. (17).

By performing an analogous derivation, the following equations are derived.

$$\delta y(S_{n,3,s}, S_{n,1,s}) = 2\{\delta y^0_{BR} - (\alpha^0_{BR} + \alpha^0_{CB}) * z_{n,1,s}\} \quad (n=2, 4, 7, 10) \quad (10)$$

$$\delta x(S_{n,4,s}, S_{n,2,s}) = -2\{(\delta x^0_{BR} + \delta x^0_{CB}) + \beta^0_{BR} * z_{n,2,s}\} \quad (n=2, 4, 7, 10) \quad (11)$$

$$\beta(S_{n,3,b}, S_{n,1,b}) = 2\beta^0_{BR} \quad (n=2, 4, 7, 10) \quad (12)$$

$$\alpha(S_{n,4,b}, S_{n,2,b}) = 2(\alpha^0_{BR} + \alpha^0_{CB}) \quad (n=2, 4, 7, 10) \quad (13)$$

$$\delta y(S_{n,3,s}, S_{n,1,s}) = -2\{(\delta z^0_{BR} + \delta x^0_{CB}) - 2\beta^0_{BR} * z_{n,1,s}\} \quad (n=3, 6, 9, 12) \quad (14)$$

$$\delta x(S_{n,4,s}, S_{n,2,s}) = 2\{(-\delta z^0_{BR} + \delta x^0_{CB}) + \beta^0_{BR} * z_{n,2,s}\} \quad (n=3, 6, 9, 12) \quad (15)$$

$$\gamma(S_{n,4,s}, S_{n,3,s}) = -2\alpha^0_{BR} \quad (n=3, 6, 9, 12) \quad (16)$$

$$\delta z(S_{n,4,b}, S_{n,1,b}) = -2\delta x^0_{BR} - (\gamma^0_{BR} - \alpha^0_{CB}) x_{n,4,b} + \beta^0_{BR} \cdot y_{n,1,b} \quad (n=3, 6, 9, 12) \quad (17)$$

$$\alpha(S_{n,4,b}, S_{n,2,b}) = -2(-\gamma^0_{BR} + \alpha^0_{CB}) \quad (n=3, 6, 9, 12) \quad (18)$$

The error sources in Table 1 can be identified by applying the least squares method to Eqs. (10) to (18) for each set (e.g., n=2 and 3 for the first set).

4. Case study

4.1 Experimental setup

The present test was carried out on a vertical machining center, NMV3000DCG from DMG Mori Co., Ltd., which has the configuration as shown in Fig. 3. Figure 7 shows the finished test piece, and Fig. 8 shows the machining test setup. The tool is a solid carbide radius end mill with DLC (diamond-like carbon) coating, ϕ10×R1.0, and the tool extension is 80 mm. The workpiece consisted of aluminum alloy (JIS A5052), the spindle speed was 6,350 min^{-1}, the feed rate was 1,700 mm/min, and the cutting fluid consisted of oil mist. Each face was finished with a radial cut depth of 0.1 mm, and it had an axial cut depth of 0.1 mm (see Fig. **9**). The machining conditions should be properly chosen such that the influence of the chatter, burr, tool deflection, and the runout on the finished surfaces is minimized. The machining of each set required three steps, and the machining took approximately 8 min. After machining each set, the spindle was warmed up by performing rotations at 6,350 min^{-1} for 15 min. In other words, each set was machined for approximately 23 min. The entire test (four sets) took approximately 80 min. The machine controller's thermal compensation was turned off throughout the test. Table 5 shows the temperatures measured with thermocouples that were attached to a) the Z-axis servo motor frame, b) the spindle unit frame near its front bearing, c) the machine table, and d) the air near the test piece. The spindle temperature increased by 1.4 °C in 70 min. Only the temperature on the spindle unit frame, not its inside, was measured. This may not directly show the spindle's thermal deformation.

The same test was conducted four times on the same machine tool under the same machining conditions (called test pieces #1 to #4). Test piece #1 was machined in October 2018, and test pieces #2 to #4 were machined on different days in October 2020.

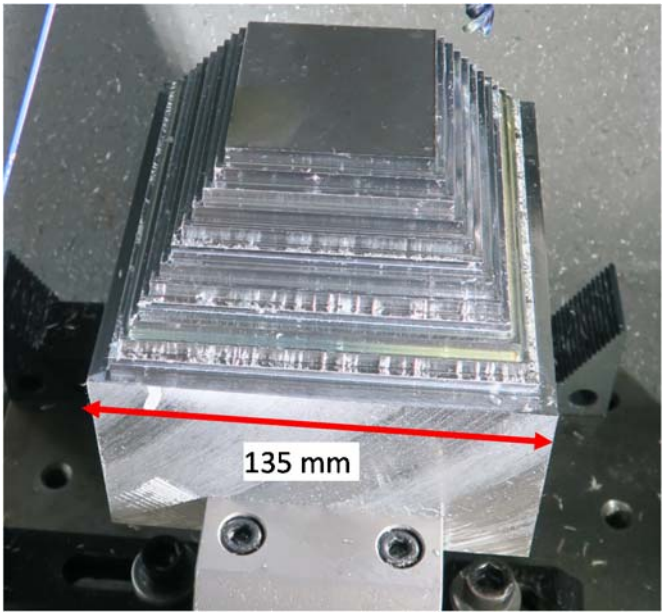

Figure 7. Finished test piece.

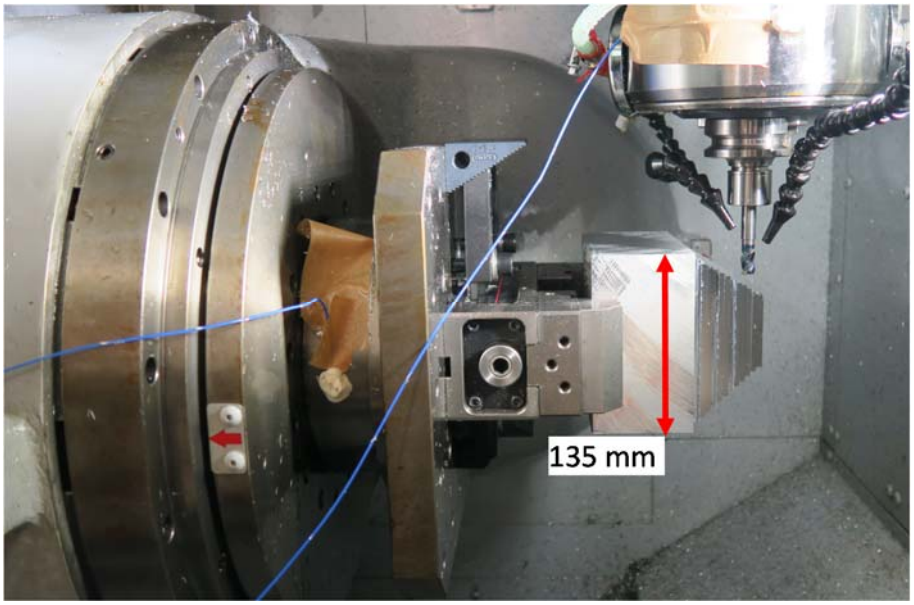

Figure 8. Machining test setup (at B=-90°).

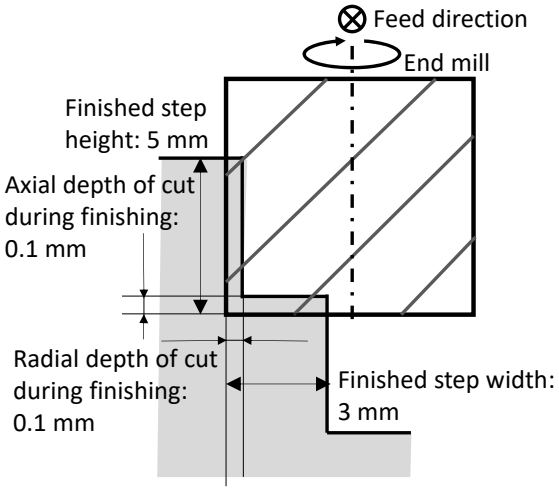

Figure 9. Radial and axial cut depths during the finishing.

Table 5. Temperatures measured in the machining test.

	Temperature in °C when starting the machining of			
	Set 1	Set 2	Set 3	Set 4
Time	0	22 min	47 min	70 min
On Z-axis servo motor frame	31.1	32.5	33.5	33.8
On the spindle unit frame near the front bearing	17.9	18.9	19.3	19.1
On the machine table	18.9	19.1	19.3	19.5
In the air (near the test piece)	19.7	19.6	19.8	20.0

4.2 Test result

Figure 10 shows the measured geometric errors for test piece 1 that was finished. In this experiment, they were measured with a touch-trigger probe (Renishaw OMP-400 with a ϕ2 ruby ball stylus probe with a length of 70 mm) on the same machine without unclamping the finished test piece after the machine sufficiently cooled. The probed pitch, p in Fig. 5, was 3 mm for test piece #1, and 6 mm for test pieces #2 to #4. According to the manufacturer's datasheet, the unidirectional repeatability of Renishaw OMP 400 is 0.35 μm (for a stylus length of 100 mm). Its 3D lobing in the X, Y, and Z directions is ± 1.75 μm (for a stylus length of 100 mm). However, its directional pre-travel difference was calibrated in advance using a precision sphere according to the standardized procedure and was compensated for by canceling its influence from the probed displacement. The "evaluation items" in Fig. 10 are shown in Table 3. Their changes with the sets, n=1 to 4, show the thermal influence. In test piece #1, the third step of Set 4 was not machined since it was out of the X-axis stroke at B = ±90°. This problem was solved for test pieces #2 to #4; thus, all 12 steps were machined.

The position error in Y of $S_{n,3,s}$ to $S_{n,1,s}$, $\delta y(S_{n,3,s}, S_{n,1,s})$, and the position error in X of $S_{n,4,s}$ to $S_{n,2,s}$, $\delta x(S_{n,4,s}, S_{n,2,s})$, for the third step in each set (n=3, 6, 9, 12), were initially larger for the first set (-91 and -108 μm, see Fig. 10 c) and showed larger changes in Sets 1 to 3 (changed by 20 and 22 μm, see Fig. 10 c). As formulated in Eqs. (14) and (15), their major cause is the position error in Z of the B-axis, $\delta z_{BR}{}^0$. Their larger initial values were likely caused by a calibration error of the tool length. Their change was caused mainly by the machine structure's thermal deformation in the Z-direction. The thermal change in the tool length can also contribute to this.

Figure 11 shows the identified position and orientation errors of the rotary axis average lines, which are identified by applying the algorithm that is proposed in Section 3.3, and their change to Sets 1 to 4 in the thermal machining test. All the identified values for test pieces #1 to #4 are shown. The proposed test enables a user to numerically observe how the rotary axis position and the orientation change from Sets 1 to 4 due to the thermal influence. From Fig. 11, the following can be observed:

- Overall, on this machine, the thermal influence on the position and orientation errors of the rotary axis average lines was not significant. The change in the position errors (a to d in Fig. 11) from Sets 1 to 4 was smaller than 5 μm in most cases. The change in the orientation errors (e to h in Fig. 11) was 50 μm/m in most cases. Their influence on the finished test piece's geometries is proportional to the test piece size (e.g., 58.7 to 24.7 mm for its width). This indicates that the influence of the thermal change in the orientation errors is at a maximum of 5 to 10 μm.
- In Fig. 11c, the Z position error of the B-axis average line, $\delta z_{BR}{}^0$, is larger in test piece #1 than in test pieces 2 to 4 by approximately 40 μm. This error represents the difference between the nominal Z position of the B-axis, which is stored in the machine controller, and its actual position. Between test piece #1 (in 2018) and the other test pieces (in 2020), the nominal Z position of the B-axis in the machine controller was modified by 41 μm, which clearly explains this difference.
- In Fig. 11c, the Z position error of the B-axis average line, $\delta z_{BR}{}^0$, increases by 5 to 10 μm from Set 1 to 4 for all the test pieces. When a spindle generates heat, it typically displaces a tool in the Z-direction, which changes the

Z position of the B-axis relative to the tool. The change in δz_{BR}^{0} is the most typical thermal influence of the spindle heat.

- The following three errors show a larger variation among test pieces #1 to #4: Fig. 11d (intersection error of the C- to B-axis, δx_{CB}^{0}), Fig. 11f (squareness error of the C- to X-axis at B0, β_{BR}^{0}), and Fig. 11g (parallelism error around Z of the B- to Y-axis, γ_{BR}^{0}). They have a larger uncertainty, as discussed in Section 6 and Table 3.
- The machine's geometric errors are most likely not the same for test pieces #1 to #4 due to the change in the air temperature or the machine warming-up before the thermal machining test. The difference in the identified location errors in test pieces #1 to #4 is attributed to the uncertainty discussed in Section 6 and to the change in the machine's geometric errors.

The profile of one of the finished faces, $S_{10,2,s}$, which is the side face machined at B'=C'=0°, was measured over its full length. A laser interferometer, SI-F10 by Keyence, was installed on the spindle with the same machine tool, and the finished test piece was fixed on the machine table at B=90°. A single line that was 2 mm below the step height was continuously measured (sampling time: 1 ms) by driving the machine's Y-axis. The sensor's major specifications are as follows: a measurable range of 11.8 mm ± 1.0 mm, a laser spot diameter with a reference working distance of 40 μm, and a resolution of 10 nm. Figure 12a shows the measured profile over its full length (112.7 mm). The magnified view in Fig. 12b shows the cutter marks with the period corresponding to the feed per rotation (0.28 mm/rev). Its amplitude, as well as the waviness of the lower frequency, observed in Fig. 12a, slightly influences the probed positions in comparison with the uncertainty that is shown in Table 1 (see Section 6). The profile shown in Fig. 12a may be affected by the straightness error motion of the Y-axis. In Fig. 12b, the surface roughness profile has a wavelength that corresponds to the feed per spindle revolution, which was 0.268 mm/rev. This is likely due to the tool runout to the axis of the spindle rotation.

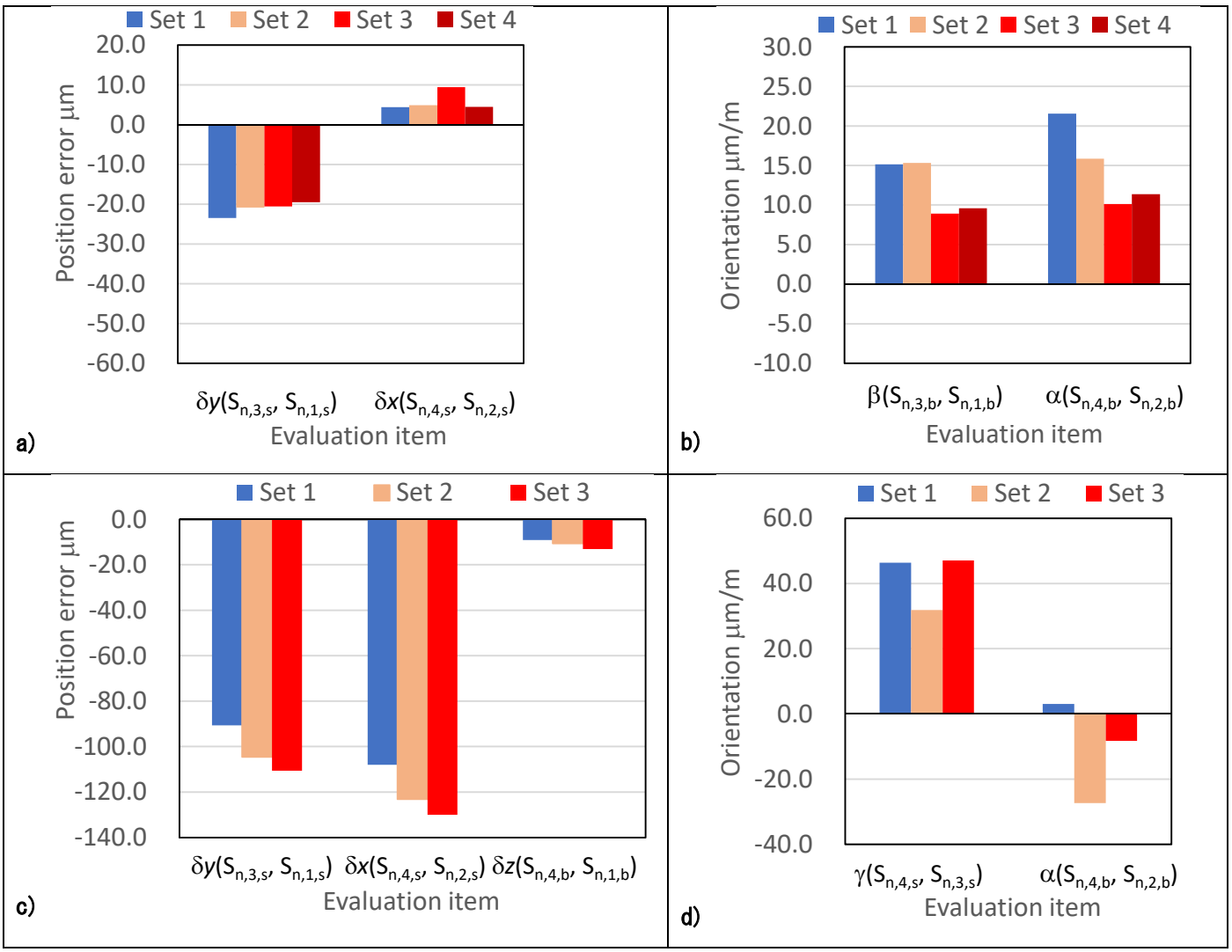

Figure 10. Measured geometric errors of the finished test piece. See Table 3 for the "evaluation items." The changes for sets 1 to 4 (3 for c and d) show the thermal influence. In addition, a) and b) show the geometric errors of the second step for each set (n=2, 5, 8, 11), and c) and d) show the geometric errors of the third step for each set (n=3, 6, 9).

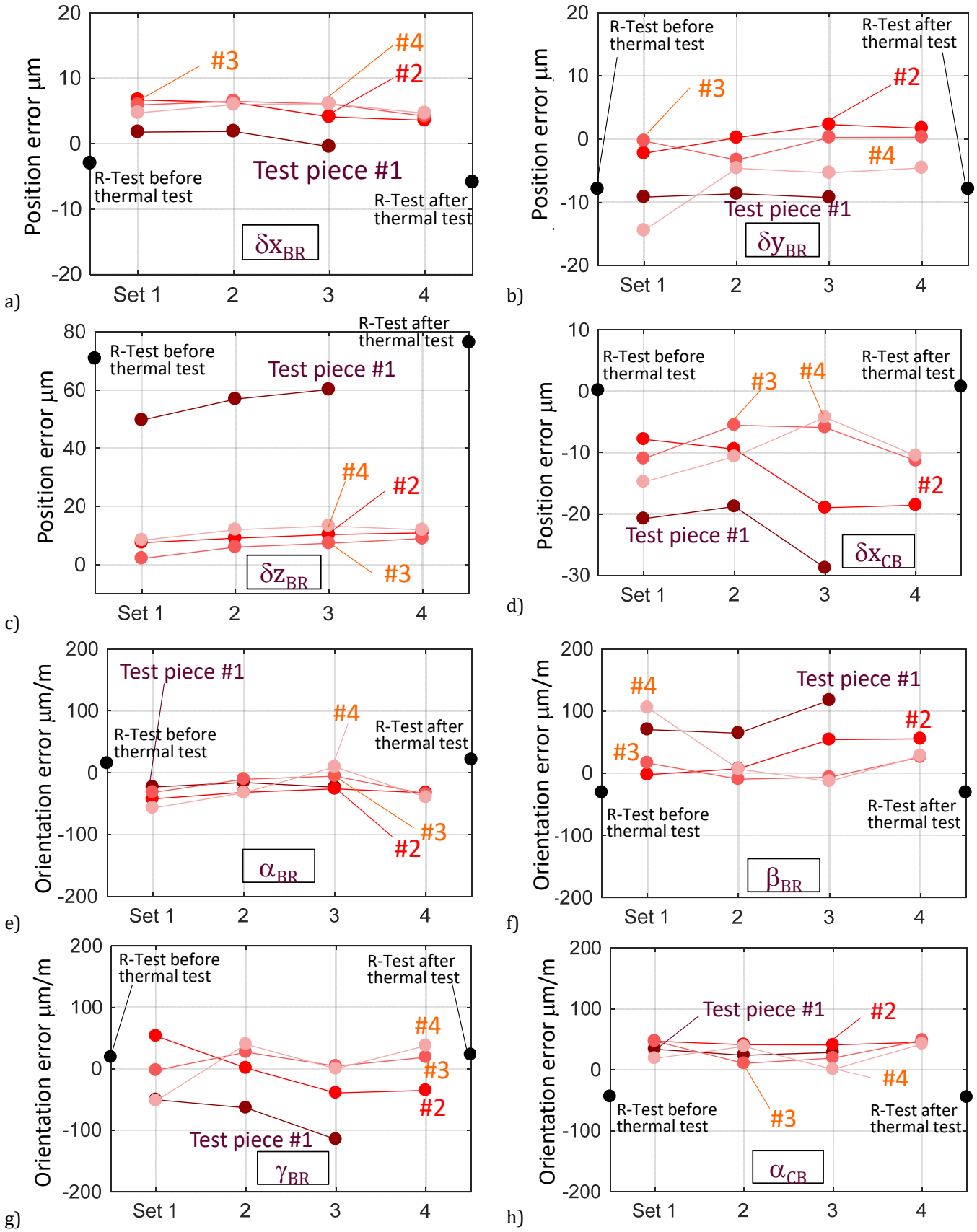

Figure 11. Identified position and orientation errors of the rotary axes average lines and their change for the thermal machining test. Sets 1 to 4 were machined every 23 min under a continuous spindle rotation. The same test was conducted four times (test pieces #1 to #4). a) δx_{BR}, b) δy_{BR}, c) δz_{BR}, d) δx_{CB}, e) α_{BR}, f) β_{BR}, g) γ_{BR}, h) α_{CB} (see Table 4 for their definitions).

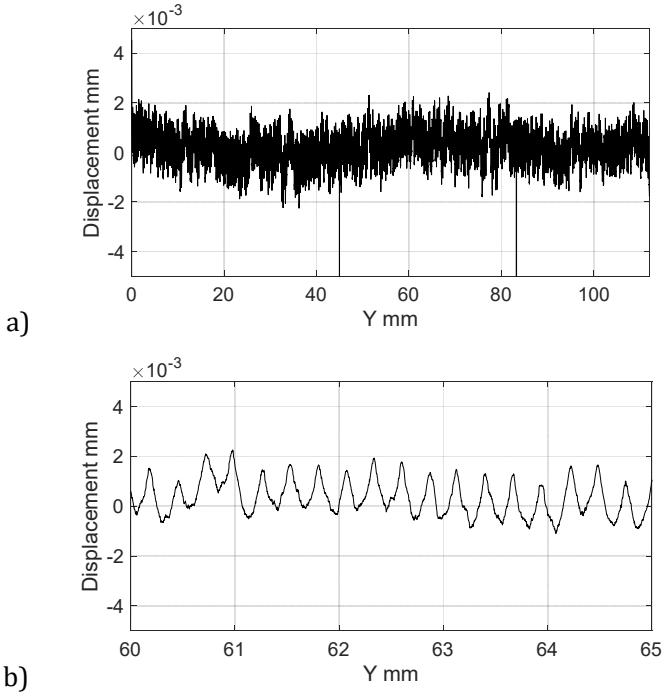

Figure 12. Profile of the machined surface ($S_{10,2,s}$) that was measured on the machine using a laser displacement sensor. a) Surface profile over the full length (112.7 mm) and b) the magnified view.

4.3 Comparison with the R-test and remarks

For comparison, the position and orientation errors of the rotary axis average lines, as shown in Table 1, were identified by the R-test. The R-test [26][29][30][31] measures the 3D displacement of the sphere that is attached to the machine spindle by a set of three displacement sensors installed on the machine table. The R-test is well established and described in ISO 10791-6 [32]. It can be performed only when the spindle stops; thus, unlike the present machining test, it may not evaluate the rotary axis location errors under the thermal conditions with a rotating spindle. This issue is discussed in [33].

Figure 13 shows the R-test setup. The R-test was performed on a different day from the machining test. The R-test cycle was first performed, then the sphere was removed, and then an end mill was installed on the spindle. Subsequently, the spindle was rotated for 80 min, which is approximately the same as the machining test. Further, the sphere was installed again on the spindle, and the R-test cycle was performed (the R-test cycle started about 10 min after the spindle stopped). In Fig. 12 a to h, the black dots ("R-test before the thermal test" and "R-test after the thermal test") represent the rotary axis location errors that are estimated by the R-test before and after the 80-min warm-up cycle. Table **6** shows the temperatures that were measured for each R-test cycle.

Tables **5** and **6** show that the thermal conditions in the machining test and R-test have some differences. The difference in the estimates that are displayed in Fig. 12 in the initial test for both tests ("Set 1" in the machining test and the R-test before the thermal test) may be attributed to this. On the other hand, the change that was observed in the identified rotary axis location errors before and after the machine warming-up cycle had a good match (i.e., the difference between Sets 1 and 4 in the machining test, and before and after the thermal test in the R-test). The R-test can be performed only when the spindle stops, and the temperature may quickly decrease immediately when the spindle stops. Ibaraki et al. [33] reported an experimental result that shows the position error of a rotary axis average

line, which was changed by approximately 30% in 15 min after the spindle stopped.

Remark #1 (influence of the tool deflection): The finishing conditions were chosen such that the tool deflection due to the cutting force is minimized. Furthermore, even if the tool deflection causes a geometric error for the finished test piece, its influence on the location errors for the identified rotary axis is minimal, provided that the tool deflection is constant. A constant tool deflection does not influence the test results, which is similar to the error for the calibrated tool diameter.

Remark #2 (influence of the test piece temperature): The thermal deformation of the test piece due to the cutting heat or the environment's thermal change can be an uncertain contributor. If the test piece is uniformly expanded and its influence is constant, then it would not have an influence, similar to that in Remark #1. The test piece temperature can change; however, during the machining test, its distribution is likely varied. In this experiment, the test piece temperature was not measured.

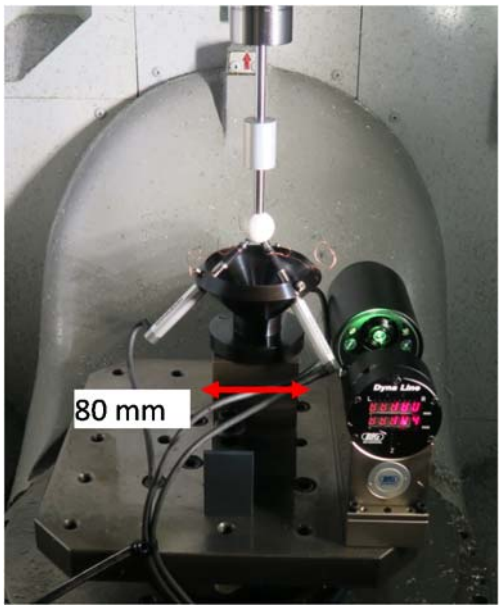

Figure 13. R-test setup.

Table 6. Temperatures in °C measured with the R-test.

	Before warm-up	After warm-up
On Z-axis servo motor frame	28.4	31.8
On the spindle unit frame near the front bearing	12.4	15.3
In the air (near the test piece)	17.6	19.4

5. Discussion: potential applications of the proposed test

The present test is designed such that errors are caused in the machine's kinematics, as described in Table 1. They can be separately analyzed from the geometric errors of the finished test piece in Table 3. For example, in the

experimental test piece, as shown in Fig. 6, a machine user may experience difficulty seeing why $\delta y(S_{n,3,s}, S_{n,1,s})$, the position error in Y of $S_{n,3,s}$ to $S_{n,1,s}$ and $\delta x(S_{n,4,s}, S_{n,2,s})$, and the position error in X of $S_{n,4,s}$ to $S_{n,2,s}$ are significantly larger. According to Eqs. (14)(15), $\delta z_{BR}{}^0$, which is the position error in Z of the B-axis, is the major contributor, and it is most likely caused by the tool setup error (i.e., an error in the calibrated tool length). On the other hand, the change in $\delta z_{BR}{}^0$ that is observed in Table 1 shows the thermal displacement of the tool in the Z-direction in reference to the B-axis average line. From this information, a machine user may improve the tool length calibration procedure. A machine designer may use this information to improve the machine design. This study contributes to the formulation of the present test for analytical testing, which can benefit machine tool users and builders.

Numerical compensation for the position and orientation errors of the rotary axis average lines, which are defined in Table 1, is possible for many commercial CNC (computer numerical control) systems [34][35]. When the machine can be assumed to be thermally stable when machining the last set (Set 3 in Table 1), it is reasonable to compensate for the identified errors from this set. A recent study [33] concluded that the position and orientation errors of the rotary axis average lines can be altered immediately after the machine spindle stops and the machine starts cooling, even when the warm-up sequence is performed for a sufficiently long time. This suggests that the non-cutting error calibration schemes (e.g., R-test [26][29][30]), may not capture the actual errors during the machining, even after a sufficient preliminary warm-up sequence. The machining test enables a user to identify the errors for the actual machining temperature; thus, the compensation can be more effective.

Many modern machine tools in the market can numerically compensate for the thermal errors. Some thermal compensations are based on the temperature measurements of the machine structure, and others are based on the operating conditions, such as the spindle rotation speed. The proposed test can be applied to check the performance of thermal compensation. Some of the latest compensation schemes [35][36] compensate for the thermal influence on the volumetric errors over the entire workspace. Unlike the conventional thermal tests in [6], which investigates the thermal displacement only at a single point, the proposed test can check the performance of the compensation more effectively.

6. Uncertainty analysis

Formulations (10)-(18) assume negligibly small linear axis error motions. As a result, it is crucial to evaluate the contribution of the linear axis error motions to the uncertainty of the identified rotary axis location errors.

The uncertainty contribution of each linear axis error motion is modeled in the same way as presented by Bringmann et al. in [37][38], presenting the uncertainty analysis for the R-test. The analogous uncertainty assessment is presented for the probing-based scheme [39] and the machining test [12]. The analogous polynomial models are employed to assess the linear axis error motions [40]. Each linear axis error motion is modeled as a Fourier series (up to the 3rd order in this evaluation). For example, the linear positioning deviation of the X-axis, E_{XX} at position x, is modeled by

$$\mathrm{E}_{XX}(x) = E_{XX,\mathrm{lin}} \cdot x + E_{XX,\mathrm{cyc}} \cdot \sum_j^3 \cos\left(j \frac{x}{X_{\mathrm{stroke}}} \pi + \phi_j\right) + E_{XX,\mathrm{rand}} \tag{19}$$

where X_{stroke} is the X-axis stroke. ϕ_j is given as a uniformly distributed random number in $[0, 2\pi]$. The linear term, $E_{XX,\mathrm{lin}}$, the amplitude of the periodic terms, $E_{XX,\mathrm{cyc}}$, and the non-periodic random term, $E_{XX,\mathrm{rand}}$, are given as a normally distributed random number with the standard deviation shown in Table 7. This is based on the accuracy-test results

from the machine manufacturer. The angular error motions were neglected, assuming a small-sized machine (the same as in [39]).

When the command TCP position (x, y, z) is given, the error motions of all the linear axes are calculated as shown in Eq. (19), and then the TCP's 3D positioning error is calculated by combining all the error motions with the machine's kinematic model [24]. The influence of the linear axis error motions on the finished test piece geometry is calculated from this. In addition, the probing uncertainty, the influence of the surface finish, and the unrepeatable error motions of the rotary axes are modeled as a uniformly distributed random number in [-2.0, +2.0] μm. The radial, axial, tilt, and angular positioning error motions of the rotary axes can influence the uncertainty; however, this uncertainty assessment focuses mainly on the influence of the linear axis error motions. Furthermore, the error motions of the rotary axes only contribute at C'=0°, 90°, 180°, 270° and B'=-90°, 0°, 90°; thus, harmonic modeling as demonstrated in Eq. (19) is not justified. Therefore, their influence is included in the assessment as a uniformly distributed random error.

In Table 1, the "uncertainty" shows the uncertainty (coverage factor, k=2) that is evaluated by applying the Monte Carlo simulation [41] applied to the formulations in Section 3.

A relatively large uncertainty can be observed with angular errors β_{BR}^0 and γ_{BR}^0 in Table 1. It can be reduced by increasing the size of the test piece. For example, in Eq. (17), a larger test piece increases $x_{n,4,b}$, which proportionally increases the influence of γ_{BR}^0 on $\delta z(S_{n,4,b}, S_{n,1,b})$, i.e., the position error in Z of $S_{n,4,b}$ to $S_{n,1,b}$. Furthermore, Eq. (18) indicates that γ_{BR}^0 is directly related to $\alpha(S_{n,4,b}, S_{n,2,b})$, i.e., the parallelism around X of $S_{n,4,b}$ to $S_{n,2,b}$. The influence of the linear axis error motions on the parallelism error of the finished faces may be reduced when the test piece is larger. This observation suggests that the uncertainty in the estimation of γ_{BR}^0 may be reduced by increasing the test piece's nominal size.

Remark 1 (similarity to the R-test): Many indirect calibration schemes of the rotary axis location errors, such as the R-Test, ball bar tests, and probing-based schemes (see [24]), require linear axes to be driven synchronously with a rotary axis (axes). They are essentially the same as the present machining test since the relative displacement of the tool to the worktable can be measured; none of them can measure the rotary axes alone. Therefore, the linear axis error motions can also significantly influence the uncertainty (e.g., the R-Test), as discussed in detail by Bringmann et al. [37]. The rotary axis error motions can be independently measured without driving the linear axes only when the measured target, such as a sphere in the R-test, is placed on the axis of rotation [42][43][44] or a tracking interferometer is employed [45].

Remark 2 (difference from the R-test): An essential difference between the present machining test and the R-test or the ball bar tests is that the present one identifies the orientation errors of the rotary axis average lines, namely α_{BR}^0, β_{BR}^0, γ_{BR}^0, and α_{CB}^0 in Table 1, partly from the orientation of the machined surfaces. The R-test measures the position of a sphere, and its direction cannot be measured. Instead, the R-test measures the orientation of a nominally circular trajectory of the tool with respect to the worktable. It is often easier to increase the radius of the trajectory, which may reduce the influence of the linear axis error motions on the identified orientation errors of the rotary axis average lines. On the other hand, the present machining test can directly measure the orientation of the axis of rotation for the given angular positions. Direct measurement of the axis of rotation is possible when a square target is used as

the measured target [39] rather than a sphere.

Table 7. Contribution of the linear axis error motions (standard deviation for the normal distribution).

Contributors		Standard deviation
Linear positioning deviation of X, Y, and Z axes	Linear term, e.g. $E_{XX,lin}$	0.002 mm for 100 mm
	Periodic term, e.g. $E_{XX,cyc}$	0.4×10^{-3} mm
	Random term, e.g. $E_{XX,rand}$	1.0×10^{-3} mm
Straightness deviation of X, Y, and Z axes	Periodic term, e.g. $E_{YX,cyc}$	0.5×10^{-3} mm
	Random term, e.g. $E_{YX,rand}$	1.0×10^{-3} mm
Squareness error between the two axes	Random term, e.g. $E_{C(0X)Y}$	0.003/300 rad

7. Conclusion

The position and orientation errors (location errors) of the rotary axis average lines are major errors in five-axis machining, often caused by the thermal deformation of the machine structure, typically due to environmental temperature variations or the heat generated by a rotating spindle. This study presents a machining test to evaluate the thermal influence on the position and orientation errors of the rotary axis average lines from the finished test piece geometry. The contributions of this study are summarized below:

- The machine's kinematic model indicates that the rotary axis location errors can be estimated from any test piece geometry, provided that it contains the features that are machined at different angular positions of the rotary axes. The present machining test is designed such that each face is machined at every combination of B'=-90°, 0°, and +90° and C'= 0°, 90°, 180°, and 270°. Therefore, the sensitivity of the finished test piece's geometry to the rotary axis location errors can be maximized within these angular ranges.
- By applying the five-axis kinematic model in the form of Eq. (1), the relationship between the geometric errors of the finished test piece and the rotary axis location errors can be analytically formulated. It provides an algorithm to identify the rotary axis location errors from the finished test piece geometry.
- An experimental case study demonstrated that the geometric errors for the first set of the three steps displayed rotary axis location errors during the initial state, and the second to fourth sets showed changes due to the thermal influence.
- For any identification scheme of the rotary axis location errors that are based on the measurement of the tool position relative to the work table, the linear axis error motions can serve as major uncertainty contributors. The uncertainty analysis reveals some orientation errors for the rotary axis average lines due to the limited size of the test piece.

References

[1] Mayr J, Jedrzejewski J, Uhlmann E, Donmez A, Knapp W, F. Härtig, K. Wendt, T. Moriwaki, P. Shore, R. Schmitt, C. Brecher, T. Würz, K. Wegener (2012) Thermal issues in machine tools, CIRP Annals -- Manufacturing Technology, 61 (2): 771-791

[2] Weck M, McKeown P, Bonse R, Herbst U (1995) Reduction and Compensation of Thermal Errors in Machine Tools, CIRP Annals -- Manufacturing Technology 44(2): 589-598.

[3] Bryan J (1990) International Status of Thermal Error Research, Annals of the CIRP 39(2): 645-656.

[4] Putz M, Richter C, Regel J, Bräunig M (2012) Industrial consideration of thermal issues in machine tools, Production Engineering 12(6): 723–736

[5] ISO 230-3:2007, Test code for machine tools -- Part 3: Determination of thermal effects.

[6] ISO 10791-10:2007, Test conditions for machining centres -- Part 10: Evaluation of thermal distortions.

[7] ISO 10791-7:2020, Test conditions for machining centres -- Part 7: Accuracy of a finished test piece.

[8] Bossoni S, Cupic J (2007) Test piece for simultaneous 5-axis machining, Laser metrology and machine performance VIII; 24-33.

[9] Hong C, Ibaraki S, Matsubara A (2011) Influence of position-dependent geometric errors of rotary axes on a machining test of cone frustum by five-axis machine tools, Precision Engineering. 35(1):1-11.

[10] Jiang Z, Ding J, Song Z (2015) Modeling and simulation of surface morphology abnormality of `S' test piece machined by five-axis CNC machine tool, International Journal of Advanced Manufacturing Technology, 85: 2745–2759

[11] Zhong L, Bi O, Huang N, Wang Y (2018) Dynamic accuracy evaluation for five-axis machine tools using S trajectory deviation based on R-test measurement, International Journal of Machine Tools and Manufacture, 125: 20-33

[12] Ibaraki S, Ota Y (2014), A machining test to calibrate rotary axis error motions of five-axis machine tools and its application to thermal deformation test, International Journal of Machine Tools and Manufacture, 86: 81-88.

[13] Ibaraki S, Tsujimoto S, Nagai Y, Sakai Y, Morimoto S, Miyazaki Y (2017) A pyramid-shaped machining test to identify rotary axis error motions on five-axis machine tools: Software development and a case study, International Journal of Advanced Manufacturing Technology, 94: 227-237

[14] Velenosi A, Campatelli G, Scippa A (2015) Axis geometrical errors analysis through a performance test to evaluate kinematic error in a five axis tilting-rotary table machine tool, Precision Engineering, 39: 224-233.

[15] Ibaraki S, Sawada M, Matsubara A, Matsushita T (2010) Machining tests to identify kinematic errors on five-axis machine tools, Precision Engineering, 34(3): 387-398.

[16] Jiang Z, Song B, Zhou X, Tang X, Zheng S (2015) On-machine measurement of location errors on five-axis machine tools by machining tests and a laser displacement sensor, International Journal of Machine Tools and Manufacture, 95: 1-12.

[17] Morimoto Y, Nakato K, Gontani M (2012) Accuracy Evaluation of 5-Axis Machining Center Based on Measurements of Machined Workpiece -- Evaluation of Accuracy of 5-Axis Controlled Machining Center --, International Journal of Automation Technology. 6(5): 675-68.

[18] Ibaraki S, Ibuki Y, Asano T (2019) A machining test to identify rotary axis geometric errors on a five-axis machine tool with a swiveling rotary table for turning operations, Precision Engineering 55: 22-32

[19] Arizmendi M, Jiménez A, Cumbicus WE, Estrems M, Artano M (2019) Modelling of elliptical dimples generated by five-axis milling for surface texturing, International Journal of Machine Tools and Manufacture, 137: 79-95.

[20] Wiessner M, Blaser P, Böhl S, Mayr J, Knapp W, Wegener K (2018) Thermal test piece for 5-axis machine tools, Precision Engineering, 52: 407-417.

[21] Höfer H, Wiemer H (2017) Generation of motion sequences for thermal load of machine tools, Production Engineering, 11: 75–83

[22] Ibaraki S, Okumura R (2020) Machining Tests to Evaluate Machine Tool Thermal Displacement in Z-Direction: Proposal to ISO 10791-10. International Journal of Automation Technology. 14(3): 380-385

[23] ISO 26303:2012, Machine tools -- Short-term capability evaluation of machining processes on metal-cutting machine tools.

[24] Ibaraki S, Knapp W (2012) Indirect Measurement of Volumetric Accuracy for Three-Axis and Five-Axis Machine Tools: A Review. International Journal of Automation Technology 6(2):110–124.

[25] ISO 230-1:2012, Test code for machine tools -- Part 1: Geometric accuracy of machines operating under no-load or quasi-static conditions.

[26] Ibaraki S, Oyama C, Otsubo H (2011) Construction of an error map of rotary axes on a five-axis machining center by static R-test, International Journal of Machine Tool and Manufacture 51: 190–200.

[27] ISO/CD 10791-10:2020, Test conditions for machining centres -- Part 10: Evaluation of thermal distortions.

[28] ISO 1101:2017, Geometrical product specifications (GPS) — Geometrical tolerancing — Tolerances of form, orientation, location and run-out

[29] Ibaraki S, Nagai Y, Otsubo H, Sakai Y, Morimoto S, Miyazaki Y (2015) R-Test Analysis Software for Error Calibration of Five-Axis Machine Tools --Application to a Five-Axis Machine Tool with Two Rotary Axes on the Tool Side--, International Journal of Automation Technology, 9(4): 387-395.

[30] Bringmann B, Knapp W '(2006) Model-based 'Chase-the-Ball' calibration of a 5-axis machining center,'' Annals of CIRP -- Manufacturing Technology, 55(1): 531-534.

[31] Guo J, Beaucamp A, Ibaraki S (2017) Virtual pivot alignment method and its influence to profile error in bonnet polishing, International Journal of Machine Tools and Manufacture, 122: 18-31.

[32] ISO 10791-6:2014, Test conditions for machining centres -- Part 6: Accuracy of speeds and interpolations.

[33] Ibaraki S, Inui H, Hong C, Nishikawa S, Shimoike M (2019) On-machine identification of rotary axis location errors under thermal influence by spindle rotation, Precision Engineering, 55: 42-47.

[34] Yamada Y (2012) Compensation technology for volumetric error in machine tool, Proceedings of the 15th international machine tool engineers' conference

[35] Wegener K, Weikert S, Mayr J (2016) Age of Compensation -- Challenge and Chance for Machine Tool Industry, International Journal of Automation Technology, 10(4): 609-623

[36] Gebhardt M, Schneeberger A, Weikert S, Knapp W, Wegener K, Thermally Caused Location Errors of Rotary Axes of 5-Axis Machine Tools, International Journal of Automation Technology, 8 (4) 511-522

[37] Bringmann B, Knapp W (2009) Machine tool calibration: geometric test uncertainty depends on machine tool performance, Precision Engineering 33: 524–529.

[38] Bringmann B, Besuchet JP, Rohr L (2008) Systematic evaluation of calibration methods, Annals of CIRP -- Manufacturing Technology 57(1): 529–532.

[39] Ibaraki B, Iritani T, Matsushita T (2013) Error map construction for rotary axes on five-axis machine tools by on-the-machine measurement using a touch-trigger probe, International Journal of Machine Tools and Manufacture, 68: 21-29.

[40] Li Q, Wang W, Zhang J, Shen R, Li H, Jiang Z (2019) Measurement method for volumetric error of five-axis machine tool considering measurement point distribution and adaptive identification process, International Journal of Machine Tools and Manufacture, 147: 103465.

[41] JCGM 100:2008, Evaluation of measurement data - Guide to the expression of uncertainty in measurement (GUM), BIPM.org

[42] Kenno T, Sato R, Shirase K, Natsume S, Spaan H (2020) Identification method of error motions and geometric errors of a rotary axis by R-test, International Journal of Automation Technology, 14(3): 399-408.

[43] Wang Z, Wang D, Dong H, Yu S (2019) An invariant method updating Abbe principle for accuracy test and error calibration of rotary pairs in machine tools, International Journal of Machine Tools and Manufacture, 141: 46-58

[44] Jiang X, Cripps RJ (2015) A method of testing position independent geometric errors in rotary axes of a five-axis machine tool using a double ball bar, International Journal of Machine Tools and Manufacture, 89: 151-158.

[45] Schwenke H, Schmitt R, Jatzkowski P, Warmann C (2009) On-the-fly calibration of linear and rotary axes of machine tools and CMMs using a tracking interferometer, CIRP Annals - Manufacturing Technology 58(1):477-480